THE JOURNAL OF PHYSICAL CHEMISTRY Letters

Letter

pubs.acs.org/JPCL

Assessment of Hybrid Organic–Inorganic Antimony Sulfides for Earth-Abundant Photovoltaic Applications

Ruo Xi Yang,[†] Keith T. Butler,[†] and Aron Walsh*[,†,‡]

[†]Centre for Sustainable Chemical Technologies and Department of Chemistry, University of Bath, Bath BA2 7AY, United Kingdom
[‡]Global E[3] Institute and Department of Materials Science and Engineering, Yonsei University, Seoul 120-749, Korea

ABSTRACT: Hybrid organic–inorganic solar absorbers are currently the subject of intense interest; however, the highest-performing materials contain Pb. Here we assess the potential of three Sb-based semiconductors: (i) Sb_2S_3, (ii) $Cs_2Sb_8S_{13}$, and (iii) $(CH_3NH_3)_2Sb_8S_{13}$. While the crystal structure of Sb_2S_3 is composed of 1D chains, 2D layers are formed in the ternary cesium and hybrid methylammonium antimony sulfide compounds. In each case, a stereochemically active Sb $5s^2$ lone pair is found, resulting in a distorted coordination environment for the Sb cations. The bandgap of the binary sulfide is found to increase, while the ionization potential also changes, upon transition to the more complex compounds. Based on the predicted electronic structure, device configurations are suggested to be suitable for photovoltaic applications.

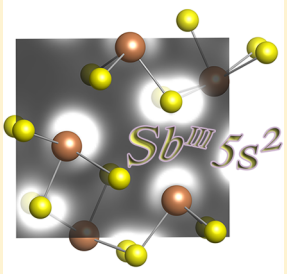

Since the development of silicon-based solar cells in the 1950s, there has been a search for new materials with direct bandgaps and high optical absorption coefficients that are cheap and easy to process. One recent success has been the development of lead halide perovskites, which have shown a rapid increase in light-to-electricity conversion efficiency from 3.8% in 2009 to 20.1% in 2015 with low-cost solution-based processing.[1−4]

An advantage of the perovskite family of compounds is that the properties are highly tunable with chemical composition. Taking the $CsPbX_3$ (X = Cl, Br, I) series for instance, these materials have an unusual electronic structure due to the Pb^{2+} configuration ([Xe] $5d^{10}6s^26p^0$). The contribution of the cation s orbital to the upper valence band results in a light hole effective mass, while the contribution of the cation p orbital to the lower conduction band results in a low bandgap (due to strong relativistic renormalization). The optical bandgap can be tuned by changing the halide component from Cl to Br to I,[5] which alters the anion component of the valence band from principal quantum number 3p to 4p to 5p, enabling compositional engineering of the physical properties.

Beyond inorganic lead halide perovskites, hybrid organic–inorganic perovskites have also attracted intense study. The methylammonium lead halide perovskites, $CH_3NH_3PbX_3$ (X = Cl, Br, I), have been used to produce high-efficiency solution-processed solar cells.[1−4] However, the intrinsic instability and potential toxicity of these materials make them less than ideal candidates for large-scale deployment of solar energy. Therefore, great efforts are being made to identify alternative lead-free materials with comparable properties and energy conversion efficiency.[6,7] Two recent examples are the layered $Cs_3Sb_2I_9$ and mixed-anion $CH_3NH_3BiSeI_2$ systems.[8,9]

Antimony sulfide (Sb_2S_3) is a semiconductor that has been studied since the 19th century owing to its occurrence as the natural mineral stibnite. It has been considered as a candidate for light-harvesting applications due to its favorable material properties.[10,11] It is reported to be an n-type semiconductor with an optical bandgap of 1.7−1.9 eV, and has a high optical absorption coefficient of 1.8×10^5 cm^{-1}(at 450 nm).[12,13] In addition, the earth-abundant nature and solution-processability of antimony sulfide are also desirable characteristics for solar energy harvesting. Importantly, Sb^{3+} has a s^2 valence electronic configuration similar to Pb^{2+}, which could provide comparable electronic features to lead halide perovskites. Hence these antimony sulfide-based materials should preserve the high dielectric constants and the associated tolerance to structural defects.[14] Unfortunately, the performance of solar cells based on Sb_2S_3 has been poor to date, with a record conversion efficiency of 6.4%,[15] which was limited by a low open-circuit voltage due to fast electron–hole recombination.[16]

In this Letter, we assess the properties of ternary and hybrid antimony sulfides in comparison to the more widely studied Sb_2S_3. The chemical series $Sb_2S_3 \rightarrow Cs_2Sb_8S_{13} \rightarrow (CH_3NH_3)_2Sb_8S_{13}$ can be considered analogous to the lead halide system $PbI_2 \rightarrow CsPbI_3 \rightarrow CH_3NH_3PbI_3$. Here the methylammonium cation ($CH_3NH_3^+$) is an isovalent replacement for Cs^+, but can significantly alter the structure and properties. We perform a first-principles investigation based on density functional theory (DFT) to shed light on the chemical trends and underlying electronic structure. The results are used to suggest an optimal combination of materials for solar cells and to provide guidance for future materials screening of hybrid semiconductors.

Crystal Structures. Sb_2S_3 adopts an orthorhombic crystal structure with space group *Pnma*, as shown in Figure 1a.[17] Due to the stereochemical activity of the Sb(III) lone pair electrons, the cation sits in a distorted square pyramidal coordination environment. The $(Sb_2S_3)_2$ building blocks form infinite 1D

Received: November 15, 2015
Accepted: December 1, 2015
Published: December 1, 2015

DOI: 10.1021/acs.jpclett.5b02555
J. Phys. Chem. Lett. 2015, 6, 5009−5014

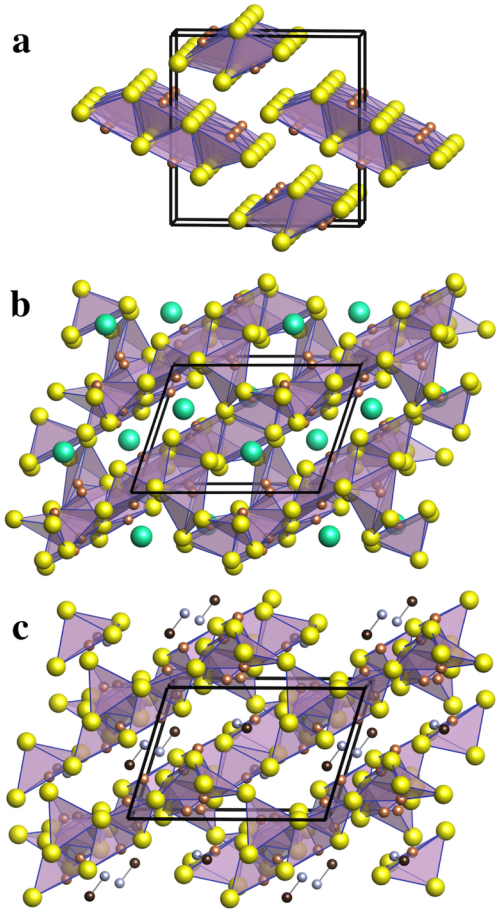

Figure 1. Representation of the crystal structures of (a) Sb_2S_3 (through ⟨010⟩), (b) $Cs_2Sb_8S_{13}$ (through ⟨100⟩), and (c) $(CH_3NH_3)_2Sb_8S_{13}$ (through ⟨100⟩). The S atoms are colored yellow, with brown Sb and green Cs. The methylammonium ions in blue (N) and dark brown (C) are drawn without hydrogen atoms for clarity. Visualization is performed using the VESTA package.[18]

chains, separated by the Sb lone pair electrons, and connected to each other by weak S−S interactions.

In contrast to the binary sulfide, multicomponent antimony chalcogenides are known to adopt chain, sheet, and three-dimensional network structures. The crystal structures of $Cs_2Sb_8S_{13}$ and $(CH_3NH_3)_2Sb_8S_{13}$, which adopt pseudo 2D sheets along (011) planes, are shown in Figure 1b,c.

The structural chemistry of $Cs_2Sb_8S_{13}$ single crystals was studied several decades ago using X-ray diffraction.[19,20] The material can be formed by the mixture of Sb_2S_3 and Cs_2S. The Cs atoms are located in the apertures between $Sb_8S_{13}^{2-}$ sheets and function as cationic bridges between them. The Sb cations are present in a mixture of distorted square pyramidal (5 Sb−S bonds) and seesaw (4 Sb−S bonds) coordination environments. The $[SbS_n]$ polyhedra share corners and edges to form infinite chains, which are linked by persulfide bonding defining the two-dimensional undulating layers. The material crystallizes in a triclinic system with the low-symmetry space group $P\bar{1}$.

In the methylammonium antimony sulfides, a similar structure is adopted, where the organic cations $CH_3NH_3^+$ sit within the heterorings built by the characteristic $[SbS_3]^{3-}$ and $[Sb_4S_7]^{2-}$ building units. The crystal is again triclinic with space group $P\bar{1}$.[21,22] The material can be grown hydrothermally from a mixture of Sb, S, and CH_3NH_2. It should be noted that the molecular cation $CH_3NH_3^+$ has a large intrinsic electrical dipole moment (ca. 2.2 D). Orientational disorder inside the aperture, which is also found in $CH_3NH_3PbI_3$,[23] could potentially result in ferroelectric or paraelectric behavior of this hybrid organic−inorganic material. Hang et al. reported a class of hybrid ferroelectrics,[24] which also includes hybrid inorganic−organic Sb based compounds, suggesting the possibility of similar behavior in the materials discussed here. The additional structural and chemical flexibility may provide physical properties for the hybrid compounds that are distinct from the purely inorganic materials.

Computational Procedure. Starting from the crystal structures determined from X-ray diffraction as discussed above, the size, shape and internal positions of the conventional units cells were fully relaxed to their equilibrium values within three-dimensional periodic boundary conditions. The total energy was calculated within the framework of Kohn−Sham DFT using a plane-wave basis set as implemented in the code VASP.[25,26]

The kinetic energy cutoff for the plane waves was set to 500 eV, and a *k*-point mesh was chosen to provide sampling of at least 25 *k*-points $Å^{-1}$. The thresholds for convergence of the total energy and forces were set to 1×10^{-6} eV and 1×10^{-2} eV/Å, respectively. Electron exchange and correlation was described within the semilocal generalized gradient approx-

Table 1. Structural and Electronic Data for the Antimony Sulfides[a]

material		*a*, *b*, *c*	E_g	Φ_{bulk}	$\Phi_{surface}$
Sb_2S_3	PBEsol	11.2, 3.8, 11.1	1.21 (Direct: 1.25)	5.56	5.46
	HSE06		1.69 (Direct: 1.72)	5.77	5.78
	Exp.	11.3, 3.8, 11.2[17]	1.54−2.24[36−45]		
	LDA[32]		1.20 (Direct: 1.29)		
	GW[32]		1.54 (Direct: 1.57)		
$Cs_2Sb_8S_{13}$	PBEsol	15.3, 11.3, 8.2	1.10 (Direct: 1.13)	4.90	4.31
	HSE06		1.82 (Direct: 1.85)	5.15	4.75
	Exp.[19]	15.4, 11.5, 8.3			
$(CH_3NH_3)_2Sb_8S_{13}$	PBEsol	15.9, 11.6, 8.1	1.28 (Direct: 1.34)	6.07	5.29
	HSE06		1.99 (Direct: 2.08)	7.01	5.79
	Exp.[22]	15.9, 11.6, 8.3			

[a]Lattice constants *a*, *b*, and *c* are given, as well as the calculated bandgap in comparison to previous theoretical and experimental studies. The bandgap values outside the parentheses refer to indirect transitions (a change in crystal momentum). Ionization potentials of both bulk and surfaces are also shown, as defined in the text. Notice that the non-local HSE06 calculated bandgap and ionization potential are always larger than the semilocal PBEsol exchange-correlation functional. All energies are given in eV, lengths in Å.

DOI: 10.1021/acs.jpclett.5b02555
J. Phys. Chem. Lett. 2015, 6, 5009−5014

imation using the PBEsol functional,[27] which accurately describes both the crystal structure and total energies in solid-state heteropolar compounds such as these. In order to provide more quantitative electronic structure information, we used a hybrid nonlocal exchange-correlation treatment that incorporated 25% screened Hartree−Fock exchange, the HSE06 functional.[28,29] In contrast to Pb halide materials, where relativistic spin−orbit coupling (SOC) strongly affects the electronic structure,[30,31] for Sb-based compounds the effect is weaker (ΔE_g^{SOC} = 20−60 meV for Sb_2S_3)[6,32] so only scalar-relativistic corrections are included in this study.

Within periodic boundary conditions the electrostatic potential of a crystal is not defined with respect to an external vacuum level, so that the absolute electronic energy levels (eigenvalues) from different calculations cannot be compared.[33] To overcome this limitation, we have generated surface terminations for each of the three materials: the well-studied (001) surface of Sb_2S_3 and the (100) surfaces of $Cs_2Sb_8S_{13}$ and $(CH_3NH_3)_2Sb_8S_{13}$. Using the package MacroDensity,[34,35] the Kohn−Sham eigenvalues of the upper valence band (ϵ_{VB}^{KS}) were aligned with respect to an external vacuum level (VL), with the surface ionization potential (Φ^{surf}) calculated according to

$$\Phi^{surf} = \epsilon_{VB}^{KS} - VL \quad (1)$$

The effect of the surface states was removed by aligning bulk and surface calculations using core-level eigenvalues (ϵ_{bulk}^{core} and ϵ_{surf}^{core}), yielding a bulk ionization potential:

$$\Phi^{bulk} = \epsilon_{VB}^{KS} - (\epsilon_{bulk}^{core} - \epsilon_{surf}^{core}) - VL \quad (2)$$

This procedure accounts for surface states created due to the under-coordination of atoms at the crystal termination.

Electronic Structure. The equilibrium crystal structures are in good agreement (within 2%) with the finite-temperature structures previously determined from X-ray diffraction (see Table 1). The calculated electronic band structures are presented in Figure 2. Multiple valleys are found in the conduction band of each material with the minimum falling away from the high-symmetry *k*-points. The fundamental bandgaps are indirect in each case, and there are small differences between the direct and indirect bandgaps ($E_g^{direct} - E_g^{indirect} < 0.1$ eV).

The predicted direct bandgaps of Sb_2S_3, $Cs_2Sb_8S_{13}$, and $(CH_3NH_3)_2Sb_8S_{13}$ are 1.72, 1.85, and 2.08 eV, respectively. Both the conduction and valence bands of Sb_2S_3 show high dispersion in reciprocal space, which is associated with light electron and hole effective masses. The range of reported optical bandgaps of Sb_2S_3 is 1.54−2.24 eV,[41−45] with differences due to data fitting procedures and sample variation, thus our calculations are at least consistent with experimental results. For the multicomponent materials, there is an increase in the magnitude of the bandgap by 0.1 and 0.3 eV for $Cs_2Sb_8S_{13}$ and $(CH_3NH_3)_2Sb_8S_{13}$, respectively. While in $Cs_2Sb_8S_{13}$ and $(CH_3NH_3)_2Sb_8S_{13}$ the valence band is relatively flat, the conduction band still exhibits large dispersion, thus we would expect enhanced n-type conductivity in these materials. The strong bonding within the (011) layers in real space can result in favorable electron transport pathways.

Analysis of the electronic density of states shows that the upper valence band of Sb_2S_3 is mainly formed by Sb 5s and partially by the S 3p orbitals, while the lower conduction band consists of mainly Sb 5p as well as minor contribution from the S 3p orbitals. The lone electron pair of Sb leads to an asymmetric electronic density at the upper valence band of Sb_2S_3. The same characteristic is also observed in antimony oxides,[46] chalcogenides[47] and even persists in the amorphous state.[48]

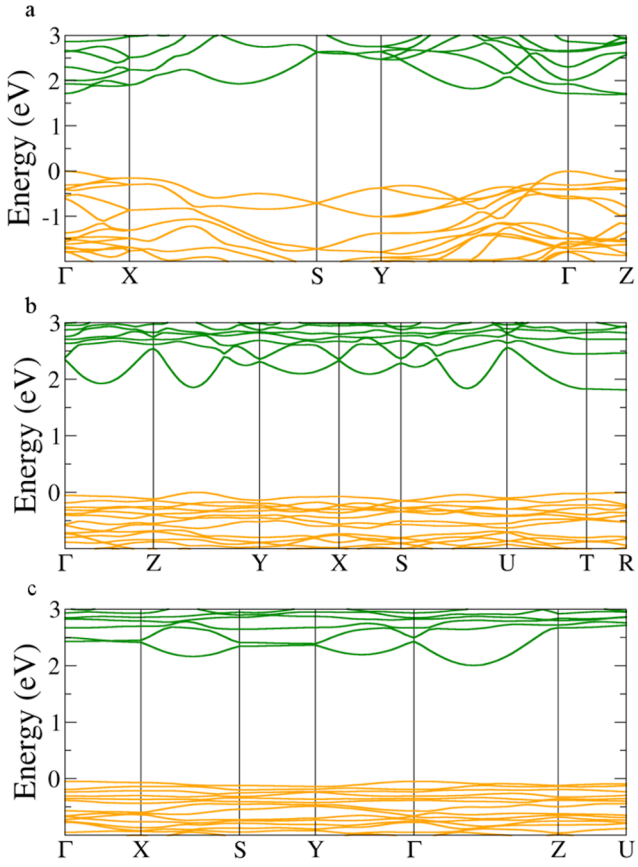

Figure 2. Electronic band structures of (a) Sb_2S_3, (b) $Cs_2Sb_8S_{13}$, and (c) $(CH_3NH_3)_2Sb_8S_{13}$ from DFT/HSE06 with scalar-relativistic effects. The special *k*-points are taken from the Bilbao Crystallographic Server.[55] The larger crystallographic cells for the cesium and methylammonium compounds result in a smaller Brillouin zone in reciprocal space and hence a higher density of bands around the Fermi level. The highest occupied state is set to 0 eV in each case.

The multivalley electronic structure of Sb_2S_3, $Cs_2Sb_8S_{13}$, and $(CH_3NH_3)_2Sb_8S_{13}$ can be regarded as a favorable characteristic for photovoltaic absorber layers, corresponding to the coexistence of strong optical absorption and slow recombination of electrons and holes.[49,50] The multivalleys provide a high electronic density of states, while maintaining band dispersion at each stationary point. There will be an associated energy loss due to thermalisation of hot carriers; however, this is balanced by the separation of electrons and holes to different wavevectors that suppresses bimolecular recombination processes. Similar band structure features are found for other lone pair materials with low symmetry crystal structures such as SnS and $CuSbS_2$.[51−54] A kinetic model of electron transport and recombination in these unconventional (nontetrahedral) semiconductors is required to provide quantitative insights into their photophysical behavior.

Absolute Electron Energies. In addition to the bulk electron distributions, the absolute electron energies are critical for application of these materials in photovoltaic devices. In particular, work function matching is required for effective

DOI: 10.1021/acs.jpclett.5b02555
J. Phys. Chem. Lett. 2015, 6, 5009−5014

electron and hole extraction from the absorber layer and to minimize resistive losses at the interfaces.

In order to calculate the ionization potential, we have cut nonpolar surface terminations and aligned the Kohn–Sham electronic eigenvalues to the vacuum (using eqs 1 and 2). The ionization potentials of the three materials are compared in Figure 3. For Sb_2S_3, the ionization potential is calculated to be

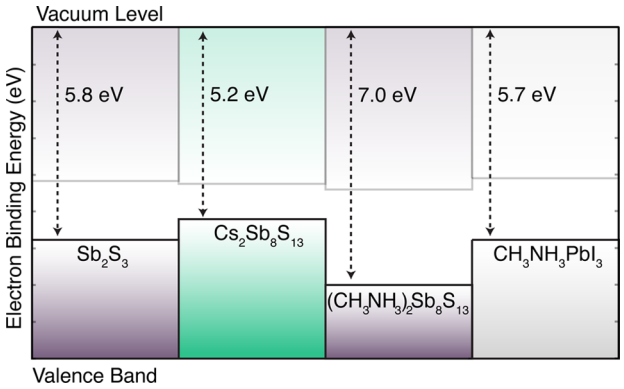

Figure 3. Predicted ionization potentials of Sb_2S_3, $Cs_2Sb_8S_{13}$ and $(CH_3NH_3)_2Sb_8S_{13}$, excluding surface and interface states, as obtained using DFT/HSE06. The values are obtained from nonpolar surfaces and using core-level alignment to the bulk valence band maximum. The value predicted for methylammonium lead iodide is shown for reference.[56]

5.77 and 5.78 eV for the bulk and (001) surface, respectively. The negligible difference indicates a chemically smooth termination without sub-bandgap surface states. The cleaved planes are weakly bound and held together by van der Waals interactions between the Sb lone pairs.

As the crystal structure gets more complex, the change of the ionization potential between the bulk and the surface increases, with 4.90 and 4.31 eV for bulk and (100) surface of $Cs_2Sb_8S_{13}$, and 6.07 and 5.29 eV for the bulk and (100) surface of $(CH_3NH_3)_2Sb_8S_{13}$. The greater difference between surface and bulk values indicates the presence of more surface states than in stibnite due to the complex chemical environment and greater amount of bond cleavage at the interface, especially for the hybrid $(CH_3NH_3)_2Sb_8S_{13}$ material. While we have confirmed there is no macroscopic dipole—the electrostatic potential plateaus to the same vacuum level on each side of the slab—the electrostatic fluctuations toward the surface are significant. This highlights a potential problem in working with low symmetry multicomponent crystals: surface and interface dipoles may be challenging to control and could require chemical passivation or modification layers in order to avoid undesirable photovoltage losses.

The ionization potential of Sb_2S_3 is similar to that of $CH_3NH_3PbI_3$, which has been calculated to be 5.7 eV.[7] Therefore, similar contacts can potentially be used in these cases including n-type oxides such as TiO_2, SnO_2, and ZnO and p-type contacts such as CuSCN or even direct contact with metals such as Mo and Au. While such device configurations should be sufficient for proof-of-principle work, other factors such as lattice matching and interfacial reactions certainly need to be considered in future studies. The substantial difference in band energies between the inorganic and hybrid compounds suggests that a modification of the electric contacts may be required to achieve high performance even within a given family of materials.

In conclusion, we have used first-principles techniques to investigate the structure and electronic properties of Sb_2S_3, $Cs_2Sb_8S_{13}$ and the hybrid compound $(CH_3NH_3)_2Sb_8S_{13}$. Each of these materials has been successfully synthesized in the past; however, their physical properties were hitherto unknown. The equilibrium crystal structure and the bandgap of Sb_2S_3 is consistent with previous experimental studies. Both $Cs_2Sb_8S_{13}$ and $(CH_3NH_3)_2Sb_8S_{13}$ show suitable bandgaps and structures for solar energy applications, and demonstrate that the bandgap can be tuned by changing the cation. The work function of the three materials has also been reported, which varies more than the bandgap, indicating the role of surface states and polarization for the multicomponent systems. A number of possible contact materials are suggested for testing photovoltaic activity.

AUTHOR INFORMATION

Corresponding Author

*E-mail: a.walsh@bath.ac.uk.

Notes

The authors declare no competing financial interest.

ACKNOWLEDGMENTS

The simulations performed in this work benefited from membership of the UKs HPC Materials Chemistry Consortium, which is funded by EPSRC grant EP/L000202. R.X.Y. is funded by ERC Starting Grant No. 277757 and K.T.B. is funded by the EPSRC grant EP/M009580/1. A.W. acknowledges support from the Royal Society. *Data access statement:* The equilibrium crystal structures and surface terminations described in this work are available in an on-line repository: https://github.com/WMD-group/Crystal_Structures

REFERENCES

(1) Jeon, N. J.; Noh, J. H.; Kim, Y. C.; Yang, W. S.; Ryu, S.; Seok, S. I. Solvent engineering for high-performance inorganic-organic hybrid perovskite solar cells. *Nat. Mater.* **2014**, *13*, 897–903.

(2) Kojima, A.; Teshima, K.; Shirai, Y.; Miyasaka, T. Organometal halide perovskites as visible-light sensitizers for photovoltaic cells. *J. Am. Chem. Soc.* **2009**, *131*, 6050–6051.

(3) Lee, M. M.; Teuscher, J.; Miyasaka, T.; Murakami, T. N.; Snaith, H. J. Efficient hybrid solar cells based on meso-superstructured organometal halide perovskites. *Science* **2012**, *338*, 643–647.

(4) Jeon, N. J.; Noh, J. H.; Yang, W. S.; Kim, Y. C.; Ryu, S.; Seo, J.; Seok, S. I. Compositional engineering of perovskite materials for high-performance solar cells. *Nature* **2015**, *517*, 476–480.

(5) Protesescu, L.; Yakunin, S.; Bodnarchuk, M. I.; Krieg, F.; Caputo, R.; Hendon, C. H.; Yang, R. X.; Walsh, A.; Kovalenko, M. V. Nanocrystals of cesium lead halide perovskites ($CsPbX_3$, X = Cl, Br, and I): novel optoelectronic materials showing bright emission with wide color gamut. *Nano Lett.* **2015**, *15*, 3692–3696.

(6) Brandt, R. E.; Stevanović, V.; Ginley, D. S.; Buonassisi, T. Identifying defect-tolerant semiconductors with high minority-carrier lifetimes: beyond hybrid lead halide perovskites. *MRS Commun.* **2015**, *5*, 265–275.

(7) Butler, K. T.; Frost, J. M.; Walsh, A. Ferroelectric materials for solar energy conversion: photoferroics revisited. *Energy Environ. Sci.* **2015**, *8*, 838–848.

(8) Sun, Y.-Y.; Shi, J.; Lian, J.; Gao, W.; Agiorgousis, M. L.; Zhang, P.; Zhang, S. Discovering lead-free perovskite solar materials with a split-anion approach. *Nanoscale* **2015**, DOI: 10.1039/C5NR04310G.

(9) Saparov, B.; Hong, F.; Sun, J.-P.; Duan, H.-S.; Meng, W.; Cameron, S.; Hill, I. G.; Yan, Y.; Mitzi, D. B. Thin-film preparation and characterization of $Cs_3Sb_2I_9$: A lead-free layered perovskite semiconductor. *Chem. Mater.* **2015**, *27*, 5622–5632.

DOI: 10.1021/acs.jpclett.5b02555
J. Phys. Chem. Lett. 2015, 6, 5009–5014

(10) Moon, S.-J.; Itzhaik, Y.; Yum, J.-H.; Zakeeruddin, S. M.; Hodes, G.; Grätzel, M. Sb_2S_3 based mesoscopic solar cell using an organic hole conductor. *J. Phys. Chem. Lett.* **2010**, *1*, 1524−1527.
(11) Choi, Y. C.; Lee, Y. H.; Im, S. H.; Noh, J. H.; Mandal, T. N.; Yang, W. S.; Seok, S. I. Efficient inorganic-organic heterojunction solar cells employing $Sb_2[S_xSe_{(1-x)}]_3$ graded-composition sensitizers. *Adv. Energy Mater.* **2014**, *4*, 1301680.
(12) Versavel, M. Y.; Haber, J. A. Structural and optical properties of amorphous and crystalline antimony sulfide thin-films. *Thin Solid Films* **2007**, *515*, 7171−7176.
(13) Messina, S.; Nair, M.; Nair, P. Antimony sulfide thin films in chemically deposited thin film photovoltaic cells. *Thin Solid Films* **2007**, *515*, 5777−5782.
(14) Zakutayev, A.; Caskey, C. M.; Fioretti, A. N.; Ginley, D. S.; Vidal, J.; Stevanovic, V.; Tea, E.; Lany, S. Defect tolerant semiconductors for solar energy conversion. *J. Phys. Chem. Lett.* **2014**, *5*, 1117−1125.
(15) Choi, Y. C.; Seok, S. I. Efficient Sb_2S_3-sensitized solar cells via single-step deposition of Sb_2S_3 using S/Sb-ratio-controlled $SbCl_3$-thiourea complex solution. *Adv. Funct. Mater.* **2015**, *25*, 2892−2898.
(16) Darga, A.; Mencaraglia, D.; Longeaud, C.; Savenije, T. J.; O'Regan, B.; Bourdais, S.; Muto, T.; Delatouche, B.; Dennler, G. On charge carrier recombination in Sb_2S_3 and its implication for the performance of solar cells. *J. Phys. Chem. C* **2013**, *117*, 20525−20530.
(17) Kyono, A.; Kimata, M.; Matsuhisa, M.; Miyashita, Y.; Okamoto, K. Low-temperature crystal structures of stibnite implying orbital overlap of Sb 5s2 inert pair electrons. *Phys. Chem. Miner.* **2002**, *29*, 254−260.
(18) Momma, K.; Izumi, F. VESTA3 for three-dimensional visualization of crystal, volumetric and morphology data. *J. Appl. Crystallogr.* **2011**, *44*, 1272−1276.
(19) Volk, K.; Schäfer, H. $Cs_2Sb_8S_{13}$, ein neuer Formel- und Strukturtyp bei Thioantimoniten. *Z. Naturforsch., B: J. Chem. Sci.* **1979**, *34*, 1637.
(20) Puls, A. Templatgestützte solvothermale synthese ein beitrag zur strukturvielfalt von thioantimonaten und thiostannaten. Ph.D. thesis, Christian-Albrechts-Universität, 2006.
(21) Lees, R. J. E.; Powell, A. V.; Chippindale, A. M. Methylammonium antimony sulfide. *Acta Crystallogr., Sect. C: Cryst. Struct. Commun.* **2005**, *61*, 516−518.
(22) Wang, X.; Liebau, F. Synthesis and structure of $[CH_3NH_3]_2Sb_8S_{13}$: A nanoporous thioantimonate(III) with a two-dimensional channel system. *J. Solid State Chem.* **1994**, *111*, 385−389.
(23) Frost, J. M.; Butler, K. T.; Walsh, A. Molecular ferroelectric contributions to anomalous hysteresis in hybrid perovskite solar cells. *APL Mater.* **2014**, *2*, 081506.
(24) Hang, T.; Zhang, W.; Ye, H.-Y.; Xiong, R.-G. Metal-organic complex ferroelectrics. *Chem. Soc. Rev.* **2011**, *40*, 3577−3598.
(25) Kresse, G.; Furthmüller, J. Efficient iterative schemes for ab initio total-energy calculations using a plane-wave basis set. *Phys. Rev. B: Condens. Matter Mater. Phys.* **1996**, *54*, 11169.
(26) Shishkin, M.; Kresse, G. Implementation and performance of the frequency-dependent GW method within the PAW framework. *Phys. Rev. B: Condens. Matter Mater. Phys.* **2006**, *74*, 035101.
(27) Perdew, J. P.; Ruzsinszky, A.; Csonka, G. I.; Vydrov, O. A.; Scuseria, G. E.; Constantin, L. A.; Zhou, X.; Burke, K. Restoring the density-gradient expansion for exchange in solids and surfaces. *Phys. Rev. Lett.* **2008**, *100*, 136406.
(28) Heyd, J.; Scuseria, G.; Ernzerhof, M. Hybrid functionals based on a screened Coulomb potential. *J. Chem. Phys.* **2003**, *118*, 8207.
(29) Heyd, J.; Scuseria, G. E.; Ernzerhof, M. Erratum: Hybrid functionals based on a screened Coulomb potential [J. Chem. Phys. 118, 8207 (2003)]. *J. Chem. Phys.* **2006**, *124*, 219906.
(30) Brivio, F.; Butler, K. T.; Walsh, A.; Van Schilfgaarde, M. Relativistic quasiparticle self-consistent electronic structure of hybrid halide perovskite photovoltaic absorbers. *Phys. Rev. B: Condens. Matter Mater. Phys.* **2014**, *89*, 155204.
(31) Even, J.; Pedesseau, L.; Katan, C.; Kepenekian, M.; Lauret, J.-S.; Sapori, D.; Deleporte, E. Solid state physics perspective on hybrid perovskite semiconductors. *J. Phys. Chem. C* **2015**, *119*, 10161−10177.
(32) Filip, M. R.; Patrick, C. E.; Giustino, F. GW quasiparticle band structures of stibnite, antimonselite, bismuthinite, and guanajuatite. *Phys. Rev. B: Condens. Matter Mater. Phys.* **2013**, *87*, 205125.
(33) Ihm, J.; Zunger, A.; Cohen, M. L. Momentum-space formalism for the total energy of solids. *J. Phys. C: Solid State Phys.* **1979**, *12*, 4409.
(34) Butler, K. T.; Hendon, C. H.; Walsh, A. Electronic chemical potentials of porous metal-organic frameworks. *J. Am. Chem. Soc.* **2014**, *136*, 2703−2706.
(35) Butler, K. T.; Buckeridge, J.; Catlow, C. R. A.; Walsh, A. Crystal electron binding energy and surface work function control of tin dioxide. *Phys. Rev. B: Condens. Matter Mater. Phys.* **2014**, *89*, 115320.
(36) Vedeshwar, A. Optical properties of amorphous and polycrystalline stibnite (Sb_2S_3) films. *J. Phys. III* **1995**, *5*, 1161−1172.
(37) Tigau, N. Structural characterization and optical properties of annealed Sb_2S_3 thin films. *Rom. J. Phys.* **2008**, *53*, 209−215.
(38) Manolache, S. A.; Duta, A. The development of crystalline Sb_2S_3 thin Films as a component of the three-dimensional (3D) solar cells. *Rom. J. Sci. Technol.* **2008**, *11*, 109−121.
(39) Krishnan, B.; Arato, A.; Cardenas, E.; Roy, T. D.; Castillo, G. On the structure, morphology, and optical properties of chemical bath deposited Sb_2S_3 thin films. *Appl. Surf. Sci.* **2008**, *254*, 3200−3206.
(40) Wang, G.; Cheung, C. L. Building crystalline Sb_2S_3 nanowire dandelions with multiple crystal splitting motif. *Mater. Lett.* **2012**, *67*, 222−225.
(41) Wang, G.; Cheung, C. L. Building crystalline Sb_2S_3 nanowire dandelions with multiple crystal splitting motif. *Mater. Lett.* **2012**, *67*, 222−225.
(42) Sun, M.; Li, D.; Li, W.; Ye, D.; Huang, H.; Fu, X. Efficient degradation of methyl orange over Sb_2S_3/TiO_2 composite under visible light irradiation. *J. Phys. Chem. C* **2008**, *112*, 18076−18081.
(43) Maghraoui-Meherzi, H.; Ben Nasr, T.; Kamoun, N.; Dachraoui, M. Structural, morphology and optical properties of chemically deposited Sb_2S_3 thin films. *Phys. B* **2010**, *405*, 3101−3105.
(44) Boldish, S. I.; White, W. B. Optical band gaps of selected ternary sulfide minerals. *Am. Mineral.* **1998**, *83*, 865−871.
(45) Nair, M.; Peña, Y.; Campos, J.; Garcia, V. M.; Nair, P. K. Chemically deposited Sb_2S_3 and Sb_2S_3-CuS thin films. *J. Electrochem. Soc.* **1998**, *145*, 2113−2120.
(46) Allen, J. P.; Carey, J. J.; Walsh, A.; Scanlon, D. O.; Watson, G. W. Electronic structures of antimony oxides. *J. Phys. Chem. C* **2013**, *117*, 14759−14769.
(47) Carey, J. J.; Allen, J. P.; Scanlon, D. O.; Watson, G. W. The electronic structure of the antimony chalcogenide series: Prospects for optoelectronic applications. *J. Solid State Chem.* **2014**, *213*, 116−125.
(48) Kim, C.-E.; Skelton, J. M.; Walsh, A.; Soon, A. Solid-state chemistry of glassy antimony oxides. *J. Mater. Chem. C* **2015**, *3*, 11349−11356.
(49) Yu, L.; Zunger, A. Identification of potential photovoltaic absorbers based on first-principles spectroscopic screening of materials. *Phys. Rev. Lett.* **2012**, *108*, 068701.
(50) Yu, L.; Kokenyesi, R. S.; Keszler, D. A.; Zunger, A. Inverse design of high absorption thin-film photovoltaic materials. *Adv. Energy Mater.* **2013**, *3*, 43−48.
(51) Vidal, J.; Lany, S.; d'Avezac, M.; Zunger, A.; Zakutayev, A.; Francis, J.; Tate, J. Band-structure, optical properties, and defect physics of the photovoltaic semiconductor SnS. *Appl. Phys. Lett.* **2012**, *100*, 032104.
(52) Banai, R.; Burton, L.; Choi, S.; Hofherr, F.; Sorgenfrei, T.; Walsh, A.; To, B.; Cröll, A.; Brownson, J. Ellipsometric characterization and density-functional theory analysis of anisotropic optical properties of single-crystal α-SnS. *J. Appl. Phys.* **2014**, *116*, 013511.
(53) Dufton, J. T.; Walsh, A.; Panchmatia, P. M.; Peter, L. M.; Colombara, D.; Islam, M. S. Structural and electronic properties of $CuSbS_2$ and $CuBiS_2$: potential absorber materials for thin-film solar cells. *Phys. Chem. Chem. Phys.* **2012**, *14*, 7229−7233.

DOI: 10.1021/acs.jpclett.5b02555
J. Phys. Chem. Lett. 2015, 6, 5009−5014

(54) Kumar, M.; Persson, C. $CuSbS_2$ and $CuBiS_2$ as potential absorber materials for thin-film solar cells. *J. Renewable Sustainable Energy* **2013**, *5*, 031616.
(55) Aroyo, M.; Perez-Mato, J.; Orobengoa, D.; Tasci, E.; De La Flor, G.; Kirov, A. Crystallography online: Bilbao crystallographic server. *Bulg. Chem. Commun.* **2011**, *43*, 183−97.
(56) Frost, J. M.; Butler, K. T.; Brivio, F.; Hendon, C. H.; Van Schilfgaarde, M.; Walsh, A. Atomistic origins of high-performance in hybrid halide perovskite solar cells. *Nano Lett.* **2014**, *14*, 2584−2590.

DOI: 10.1021/acs.jpclett.5b02555
J. Phys. Chem. Lett. 2015, 6, 5009−5014